



ELSEVIER

Contents lists available at ScienceDirect

# Applied Catalysis B: Environmental

journal homepage: [www.elsevier.com/locate/apcatb](http://www.elsevier.com/locate/apcatb)



## Catalytic steam reforming of acetic acid as a model compound of bio-oil



Francisco Guilherme E. Nogueira<sup>a</sup>, Paulo G.M. Assaf<sup>a</sup>,  
Hudson W.P. Carvalho<sup>b</sup>, Elisabete M. Assaf<sup>a,\*</sup>

<sup>a</sup> Instituto de Química de São Carlos, Universidade de São Paulo, Av. Trabalhador São Carlense, 400, 13560-970 São Carlos-SP, Brazil

<sup>b</sup> Institute for Chemical Technology and Polymer Chemistry, KIT, Engesserstrasse 20, 76131 Karlsruhe, Germany

### ARTICLE INFO

#### Article history:

Received 11 December 2013

Received in revised form 31 March 2014

Accepted 13 May 2014

Available online 24 May 2014

#### Keywords:

Steam reforming

Acetic acid

Hydrogen

Biomass

### ABSTRACT

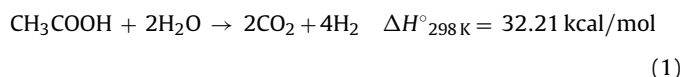
The effect of Ni catalysts promoted with Mg on catalytic activity and carbon deposition was investigated in acetic acid steam reforming. Acetic acid was chosen as representative compound for the steam reforming of bio-oil derived from biomass pyrolysis. In this study, nickel catalysts modified with Mg have been prepared by sequential impregnation method with 15 wt.% Ni and variable loadings of Mg (1–10 wt.%). The samples were characterized by X-ray fluorescence (XRF), X-ray diffraction (XRD), X-ray absorption fine structure (XAFS), high resolution transmission electron microscopy (HRTEM), specific surface area (BET) and temperature programmed reduction (TPR-H<sub>2</sub>). Steam reforming of acetic acid was conducted in a fixed bed reactor at a temperature of 500 °C and 600 °C. Under reactive conditions, the 15Ni5Mg/Al catalyst proved to be superior to the other catalysts at 600 °C at which it presented an effluent gaseous mixture with the highest H<sub>2</sub> selectivity and reasonable low coke formation.

© 2014 Elsevier B.V. All rights reserved.

### 1. Introduction

The depletion and environmental pollution from fossil fuels necessitate new energy resource development [1]. Hydrogen is recognized as the most promising alternative to fossil fuels for the future because of its cleanness, recyclability and high energy density [2,3]. Hydrogen can be produced from a variety of sources such as fossil fuels, nuclear energy, water and biomass [4]. Currently, hydrogen is produced mainly from fossil fuels; roughly 96% of hydrogen is produced by steam reforming natural gas and oil fractions [5,6]. The hydrogen production from fossil fuels presents some disadvantages such as additional consumption of fossil fuel as energy source and release of large amounts of CO<sub>2</sub> into the atmosphere [7]. In addition, the production of hydrogen from water using non-fossil primary energy sources (atomic, solar, geothermal and others) is still disadvantageous economically [8]. This is expected to result in increased usage of alternative biomass energy. In general terms, production of H<sub>2</sub> from biomass wastes can reduce waste disposal problems and substrate costs, thus becoming attractive. Moreover, it does not contribute to global warming since carbon dioxide from the atmosphere is recycled [9,10].

Hydrogen can be produced from biomass via thermochemical processes, such as flash pyrolysis, which produces mainly liquids (bio-oils), and then the bio-oils can be converted to hydrogen by catalytic steam reforming [11,12]. Steam reforming of bio-oil produced from fast pyrolysis of biomass has been described by many authors as one of the most promising and economical methods for hydrogen production [13–15]. Bio-oil is a complex mixture of organic compounds like acids, ketones, esters, alcohols, phenols and guaiacols, and its steam reforming is characterized with many difficulties; the most important is coke accumulation over the catalytic surface [16,17]. Therefore, designing efficient catalyst requires the use of model oxygenated components for preliminary tests. Acetic acid (HAc), which is soluble in water, is chosen as a model compound because it is one of the most representative constituents of bio-oil [18]. Thermodynamic calculations have proven and accounted for the feasibility of acetic acid steam reforming [19]. Stoichiometrically, steam reforming of HAc can be represented as follows (Eq. (1)):



Nickel catalysts are widely used as low-cost non-noble metal catalysts in industry for a number of chemical reaction processes. This metal is commonly employed as the active phase to conduct steam reforming of organic compounds such as methane, ethanol

\* Corresponding author.

E-mail address: [eassaf@iqsc.usp.br](mailto:eassaf@iqsc.usp.br) (E.M. Assaf).

and glycerol, due to the high C–C bond breaking activity [20–23]. Moreover, the nature of the support strongly influences the catalytic performance of supported Ni catalysts destined for steam reforming, as it affects dispersion and stability of the metal as well as may participate in the reaction [24]. Among oxide supports, alumina-based supports are commonly used for steam reforming due to their chemical and physical properties, since they have good mechanical strength and thermal stability, moreover it is possible to control their textural properties [25,26]. However, the main problem for most of the Ni catalysts supported on alumina is the high deactivation rate related to the formation of coke deposits. The deactivation can occur by covering the active phase due to encapsulating carbon and also by filamentous carbon formation [27,28]. Thus, basic additives or promoters produce highly dispersed Ni<sup>0</sup> species, and consequently, can drastically enhance the resistance to carbon deposition over Ni catalysts. Addition of alkaline earth oxides (MgO, CaO) is widely used in reforming formulations to neutralize acidity of Al<sub>2</sub>O<sub>3</sub> [29]. These basic additives, besides acting as a poison for the acid sites on alumina, also favor H<sub>2</sub>O adsorption and the OH mobility on the surface, accelerating the carbon oxidation and reducing the coke deposition [23].

In order to improve the stability of the nickel catalysts in steam reforming of acetic acid, we prepared and characterized nickel catalysts supported on  $\gamma$ -Al<sub>2</sub>O<sub>3</sub> modified by MgO used as promoter; therefore, the total amount of Mg in the nickel catalyst range from 1 to 10 wt.%. The Ni loading was fixed at 15 wt.% in all cases.  $\gamma$ -Al<sub>2</sub>O<sub>3</sub> was used as support to obtain Ni catalysts with high specific surface area. The Ni-MgO/ $\gamma$ -Al<sub>2</sub>O<sub>3</sub> catalysts were prepared by sequential impregnation method and tested in steam reforming of acetic acid at 500 and 600 °C.

## 2. Experimental

### 2.1. Catalyst preparation

Ni catalysts supported on (MgO)-modified  $\gamma$ -Al<sub>2</sub>O<sub>3</sub> were prepared by the sequential impregnation method. The  $\gamma$ -Al<sub>2</sub>O<sub>3</sub> powder (200 m<sup>2</sup> g<sup>-1</sup>; V<sub>pore</sub> = 0.60 cm<sup>3</sup> g<sup>-1</sup>; Alfa Aesar) was initially calcined under air at 500 °C for 2 h in a muffle furnace in order to remove organic impurities.  $\gamma$ -Al<sub>2</sub>O<sub>3</sub> was first impregnated with a solution of Mg(NO<sub>3</sub>)<sub>2</sub>·6H<sub>2</sub>O (Alfa Aesar) with loadings of 1, 5 and 10 wt.% of Mg, under stirring at 70 °C followed by drying overnight in air at 110 °C. The final samples (1%Mg/ $\gamma$ -Al<sub>2</sub>O<sub>3</sub>, 5%Mg/ $\gamma$ -Al<sub>2</sub>O<sub>3</sub> and 10%Mg/ $\gamma$ -Al<sub>2</sub>O<sub>3</sub>) were calcined at 650 °C for 3 h.

The modified powder with Mg was then again impregnated with the solution of Ni(NO<sub>3</sub>)<sub>2</sub>·6H<sub>2</sub>O (Vetec), under stirring at 70 °C and then dried overnight in air at 110 °C. The dried powder was finally calcined at 650 °C for 3 h to obtain the deposition of NiO on the modified  $\gamma$ -Al<sub>2</sub>O<sub>3</sub>. All the modified Ni catalysts were prepared with a load of 15 wt.% Ni. The 15 wt.% Ni with the (MgO)-modified  $\gamma$ -Al<sub>2</sub>O<sub>3</sub> were named 15Ni1Mg/Al, 15Ni5Mg/Al and 15Ni10Mg/Al. The unmodified catalyst, 15 wt.% Ni/ $\gamma$ -Al<sub>2</sub>O<sub>3</sub> was also prepared by the impregnation method for comparison to the modified Ni catalysts and named 15Ni/Al.

### 2.2. Catalyst characterization

The X-ray fluorescence analyses (XRF) were carried out using a Rigaku (RIX 3100) wavelength dispersive X-ray fluorescence spectrometer equipped with an Rh X-ray tube, 4 kW generator and 8 position crystal changer. The crystalline structure of the catalysts was analyzed by X-ray diffraction (XRD) spectra, data were collected using X'Pert Pro Multi-purpose X-ray diffraction (MPD) system employing Cu K $\alpha$  radiation ( $\lambda$  = 0.154 nm) operated at 40 mA and 45 kV. To determine the crystallite size Scherrer

equation was used [30]. Particle sizes were estimated from the peak width at half height relative to the crystallographic plane Ni (2 0 0) of the metallic nickel after correcting for instrumental broadening effects. XAS measurements at the Ni K-edge were performed at the Laboratório Nacional de Luz Síncrotron-LNLS using the XAS F1 beam line. The XAS was analyzed using Athena and Artemis IFEFFIT software packages [31]. The spectra were energy calibrated using a Ni foil as reference, they were then normalized and the background extracted. Structural models were built and the respective theoretical backscattering amplitudes and phases were calculated by FEFF6. Then the theoretical data were adjusted to the experimental by a least square method. This procedure allowed the determination of the coordination number (*N*), bond distances (*r*) and mean square deviation of interatomic distances ( $\sigma^2$ ). The amplitude reduction factor was obtained by refining a NiO reference sample, and the value found was applied to the others. The absolute misfit between theory and experiment is expressed by  $\rho$  [32] (Eq. (2)), where:

$$\rho = 100 \times \sum_{i=1}^{N_{pts}} \frac{[Im(\chi_{\text{experiment}}(R_i) - \chi_{\text{theory}}(R_i))]^2 + [Re(\chi_{\text{experiment}}(R_i) - \chi_{\text{theory}}(R_i))]^2}{[Im(\chi_{\text{experiment}}(R_i))]^2 + [Re(\chi_{\text{experiment}}(R_i))]^2} \quad (2)$$

The specific surface area (BET) was estimated from the N<sub>2</sub> adsorption/desorption isotherms at liquid nitrogen temperature (77 K), using a Quantachrome Nova 1200 instrument. Prior to the analysis, the fresh catalyst was pre-treated under vacuum at 573 K for 3 h. Temperature programmed reduction (TPR) tests were carried out in pulse chemisorptions system ChemiSorb 2750 (Micromeritics, USA) with a TCD detector at the heating rate of 10 °C min<sup>-1</sup>. TPR was carried out from 50 °C to 1000 °C in 10% H<sub>2</sub> in Ar at a flow rate of 20 mL min<sup>-1</sup>. The SEM images were obtained on a LEO 440 equipment provided with an OXFORD Instruments detector, the electron beam operating at 15 kV. Transmission electron microscopy (TEM/HRTEM) images were obtained with a FEI TECNAI G20 F20 microscope operating at 200 kV. The size distribution was determined by counting at least 50 particles.

### 2.3. Catalytic experiments

The catalytic tests for the acetic acid steam reforming were carried out using a tubular quartz reactor, containing 100 mg of catalyst. Before the reforming reactions, the catalysts were reduced with hydrogen (30 mL min<sup>-1</sup>) at 750 °C for 1 h, to activate the catalyst. Aqueous solution of acetic acid 2:1 (H<sub>2</sub>O:CH<sub>3</sub>COOH) molar ratio was fed supplied by a piston pump resulting in a speed of 0.25 mL h<sup>-1</sup>. The reactions were carried out at temperatures of 500 °C and 600 °C to evaluate the variation in the conversion and the selectivity of the products as a function of temperature. The product composition was recorded over 6 h of reaction. The stability test of the catalyst during the steam reforming of acetic acid was performed at 600 °C for the 15Ni5Mg/Al catalyst for a period of 24 h. The gaseous products were analyzed in-line by gas chromatography in a CG-3800 Varian chromatograph with two columns in parallel, packed with Porapak N and Molecular Sieve 13X, each equipped with a TCD at the exit. The selectivity (*S<sub>i</sub>*) of each product (*i* = H<sub>2</sub>, CH<sub>4</sub>, CO<sub>2</sub>, or CO) was calculated by the following equation (Eq. (3)):

$$S_i = \frac{\text{mol}_i \text{ produced}}{\text{mol}_{\text{acetic acid converted}}} \quad (3)$$

At the end of reaction, the condensed liquid products were collected and analyzed by gas chromatography (Hewlett Packard 5890), with an HP-FFAP capillary column (25 m × 0.2 mm i.d.) and FID detector. During the sample preparation, the solution was kept at a temperature under 283 K, to avoid any liquid product evaporation. The total acetic acid conversion during the test was taken

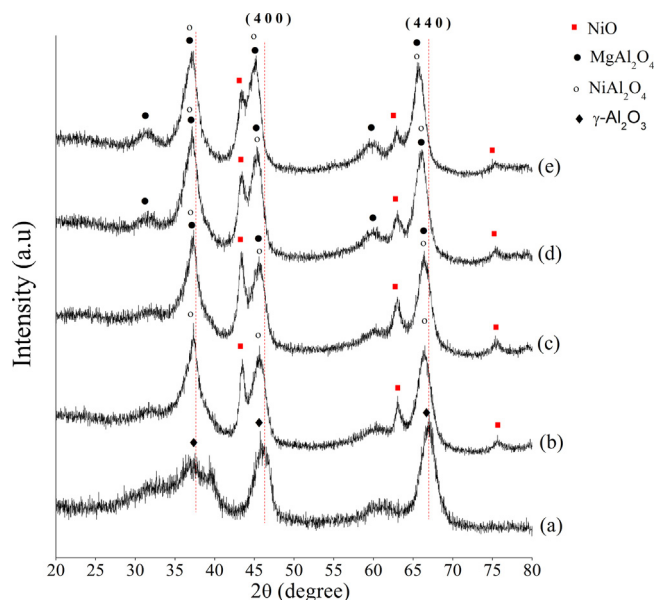


**Fig. 1.** XRD diffraction patterns of catalysts calcined at 650 °C for (a)  $\gamma$ - $\text{Al}_2\text{O}_3$  support, (b) 15Ni/Al, (c) 15Ni1Mg/Al, (d) 15Ni5Mg/Al and (e) 15Ni10Mg/Al.

as the total volume of acetic acid fed to the reactor minus the total volume of condensed acetic acid, expressed as a percentage of the total fed volume. Carbon deposited during the reaction on used catalysts was evaluated by TGA on a Mettler Toledo TGA/DSC1 thermobalance under air flow ( $50 \text{ mL min}^{-1}$ ) with a heating rate of  $10^\circ \text{C min}^{-1}$  up to  $1000^\circ \text{C}$ .

### 3. Result and discussion

#### 3.1. Catalyst characterization

##### 3.1.1. XRF analysis

The results of X-ray fluorescence showed that the contents were very close to the nominal composition (Table 1), indicating that there was no loss of Ni and Mg by the sequential impregnation method.

##### 3.1.2. XRD analysis

The XRD diffraction patterns for calcined and reduced catalysts are shown in Figs. 1 and 2 and their textural properties in Table 1. The typical diffraction peaks of  $\gamma$ - $\text{Al}_2\text{O}_3$  support at  $2\theta = 36.9^\circ$ ,  $46.8^\circ$  and  $66.7^\circ$  (JCPDS 86-1410) virtually coincided with those of the  $\text{NiAl}_2\text{O}_4$  and  $\text{MgAl}_2\text{O}_4$  spinel-like phase, making it difficult to distinguish the diffraction peaks [33,34]. From XRD (Fig. 1a and b) the peak at  $36.9^\circ$ ,  $46.5^\circ$  and  $66.7^\circ$  for the  $\gamma$ - $\text{Al}_2\text{O}_3$  support and the 15Ni/Al catalyst is indistinguishable by XRD due to overlap of the crystalline phases of  $\gamma$ - $\text{Al}_2\text{O}_3$  and the  $\text{NiAl}_2\text{O}_4$  spinel [35]. However, when the nickel was loaded on the support, the main diffraction peak of  $\gamma$ - $\text{Al}_2\text{O}_3$  shifted to lower angles (Fig. 1b); this may be due to

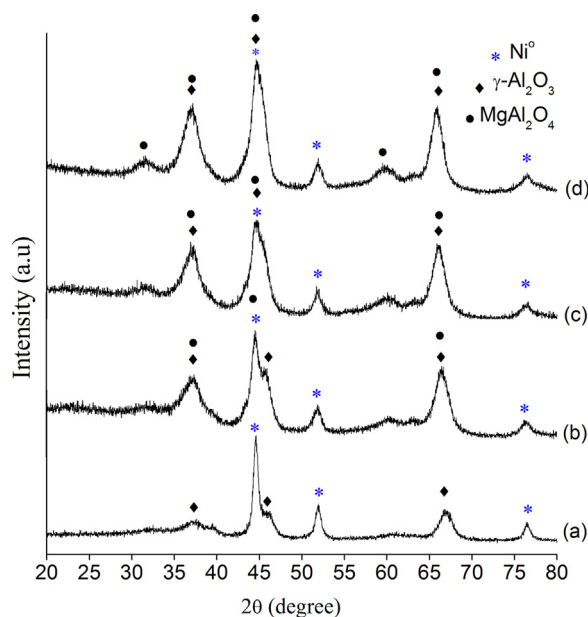


**Fig. 2.** XRD diffraction patterns of catalysts reduced at 750 °C for 1 h: (a) 15Ni/Al, (b) 15Ni1Mg/Al, (c) 15Ni5Mg/Al and (d) 15Ni10Mg/Al.

the diffusion of NiO particles into the support structure to form the  $\text{NiAl}_2\text{O}_4$  phase [36]. In addition, with increased Mg content the position of (440) and (400) peaks of the 15Ni5Mg/Al and 15Ni10Mg/Al catalyst (Fig. 1d and e) shifted to the low diffraction angles compared to that of the unmodified catalyst (15Ni/Al). This might be an indication of  $\text{MgAl}_2\text{O}_4$  phase formation, in which, the cation  $\text{Mg}^{2+}$  incorporates into the modified catalysts [37]. The ionic radius of magnesium is higher than that of aluminum, and therefore, its incorporation leads to a lattice expansion of alumina, resulting in a shift of the diffraction peak [38]. For all calcined catalysts, there are four diffraction peaks at about  $2\theta = 37.1^\circ$ ,  $43.3^\circ$ ,  $63^\circ$  and  $75.3^\circ$  attributed to the NiO phase. The NiO peak at  $2\theta = 37.1^\circ$  is more difficult to be detected due to the overlap with the  $\text{MgAl}_2\text{O}_4$ ,  $\text{NiAl}_2\text{O}_4$  and  $\gamma$ - $\text{Al}_2\text{O}_3$  peak.

XRD analysis of reduced catalysts at 750 °C (Fig. 2) showed that all samples presented diffraction peaks at  $2\theta = 44.4^\circ$ ,  $51.7^\circ$  and  $76.3^\circ$  corresponding to metallic  $\text{Ni}^0$  phases [39]. In addition, the intensities of the lines corresponding to  $\text{NiAl}_2\text{O}_4$ ,  $\gamma$ - $\text{Al}_2\text{O}_3$  and  $\text{MgAl}_2\text{O}_4$  (Fig. 2) slightly decreased after the reduction process, suggesting that the  $\text{Ni}^{2+}$  in the spinel phase has been reduced to  $\text{Ni}^0$ . The mean particle size was calculated from the  $\text{Ni}^0$  (200) peak according to Scherrer's equation [40]. Particle size of metallic Ni in the reduced catalyst modified with Mg was much smaller than that in the reduced unmodified 15Ni/Al catalyst (Table 1). This indicates that the addition of Mg prevents the sintering process and favors the dispersion of the Ni particles, even after the high-temperature reduction process [41]. Moreover, no reflections belonging to transition aluminas were observed on the

**Table 1**  
Physicochemical properties of catalysts.

Catalysts	Ni <sup>a</sup> (wt.%)	Mg <sup>a</sup> (wt.%)	$S_{\text{bet}}$ ( $\text{m}^2 \text{g}^{-1}$ )	$V_{\text{pore}}^b$ ( $\text{cm}^3 \text{g}^{-1}$ )	$d_{\text{Ni}}^c$ (nm)	$D_m$ (%)
15Ni/Al	15.7	–	141	0.44	11.2	9.2
15Ni1Mg/Al	15.6	1.1	139	0.60	8.8	11.5
15Ni5Mg/Al	15.5	4.3	125	0.44	8.8	11.4
15Ni10Mg/Al	15.5	9	107	0.37	8.6	11.7

<sup>a</sup> XRF analysis.

<sup>b</sup> Calculated through the BJH desorption.

<sup>c</sup> Calculated from XRD measurements for reduce catalysts.

( $D_m$ ) metallic dispersion.

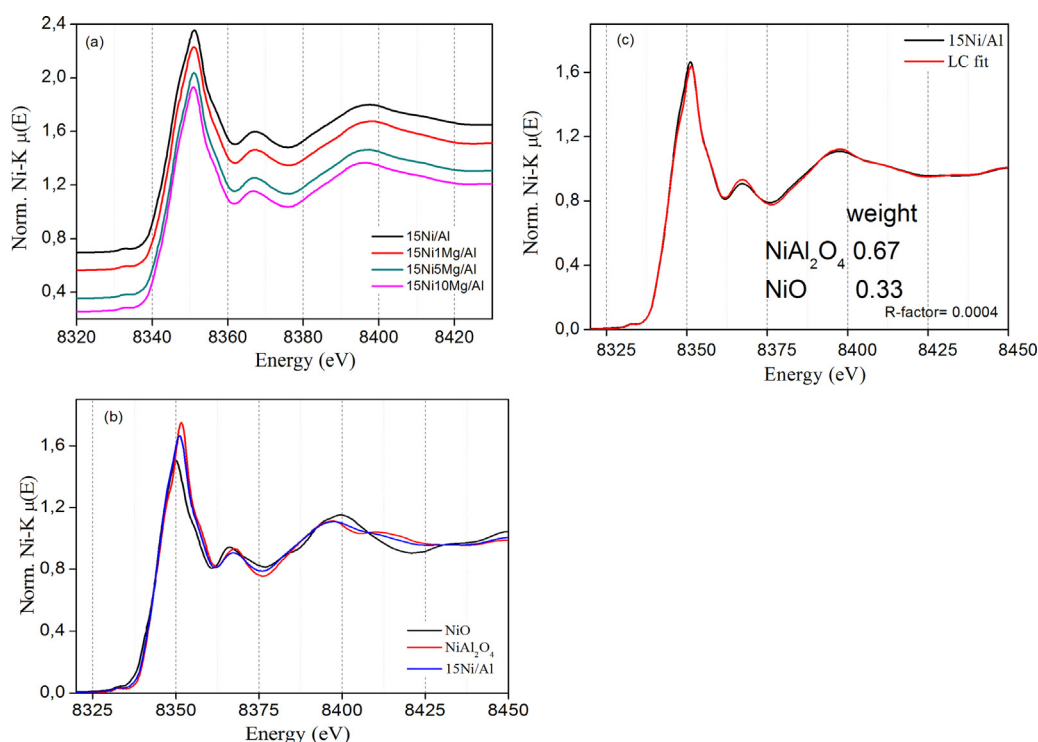


**Fig. 3.** Ni-K near edge absorption spectra, (a) spectra of undoped and Mg promoted catalyst; (b) NiO, NiAl<sub>2</sub>O<sub>4</sub> and 15Ni/Al catalyst, (c) linear combination describing the spectrum of 15Ni/Al catalyst.

reduced catalysts, indicating that the alumina transformations were not promoted at the temperatures employed in the reduction treatment.

The metallic dispersion was estimated using the X-ray diffraction (XRD) according to following equation:  $D_m = 101/d_{Ni}$ , where  $D_m$  is the metallic dispersion,  $d_{Ni}$  is the crystallite size expressed in nm and the constant (1 0 1) was calculated assuming that the nickel particles have a spherical geometry and that the density of nickel particles in a polycrystalline surface is  $1.54 \times 10^{19}$  atoms Ni m<sup>-2</sup>. Several studies have demonstrated that the metallic dispersion values obtained by chemisorption satisfactorily approximate the estimates obtained by XRD [42–45]. The metallic dispersion and the crystallite size in the catalysts promoted with Mg are presented in Table 1. There was an increase in the nickel dispersion with addition of magnesium in relation to the 15Ni/Al catalyst. Similar results were obtained by Carvalho et al. [46] in which the authors found that the addition of magnesium as a promoter significantly reduced the acidity of the support and increased the metal dispersion. According to Zhang et al. [47] the addition of basic oxides such as MgO, prevents the agglomeration of nickel metal on the support, increasing dispersion.

### 3.1.3. XAFS data analysis

**3.1.3.1. Ni local chemical environment.** Fig. 3a points out that the Ni-K near edge structure spectra presents the same features for all catalysts calcined at 650 °C, which leads to the assumption that the Ni local chemical environment should also be similar, independent of the catalyst chemical composition.

These spectral features are close to those presented by the NiAl<sub>2</sub>O<sub>4</sub> reference spectrum, as shown by Fig. 3b. A more quantitative approach, using a linear combination method, reveals that the 15Ni/Al spectrum may be described as a mixture of 67% of NiAl<sub>2</sub>O<sub>4</sub> and 33% of NiO (Fig. 3c). It does not necessarily means that the 15Ni/Al catalyst is a physical mixture of these two references, but the local order of Ni in the catalyst may be similar to the one presented by the references.

Fig. 4 presents the EXAFS spectra for NiO, NiAl<sub>2</sub>O<sub>4</sub> and 15Ni/Al. Many of the oscillations found for the catalyst are in phase with those shown by NiO. However in the regions highlighted by the arrows, between 8 Å<sup>-1</sup> and 9 Å<sup>-1</sup>, the oscillations of 15Ni/Al are dumped close to zero. In this same region the EXAFS spectrum of NiAl<sub>2</sub>O<sub>4</sub> is completely in phase opposition to NiO. This led us to conclude, corroborating the LC combination results, that the local chemical environment of the catalyst present may be related to NiO and NiAl<sub>2</sub>O<sub>4</sub>.

Intending to gain deeper information on Ni local structure we have refined the EXAFS spectra for the catalysts. Two models were assumed:

- Ni in a chemical environment similar to NiO, it means, coordinated by 6 oxygen atoms at the first shell and 12 Ni atoms at the second shell [48];

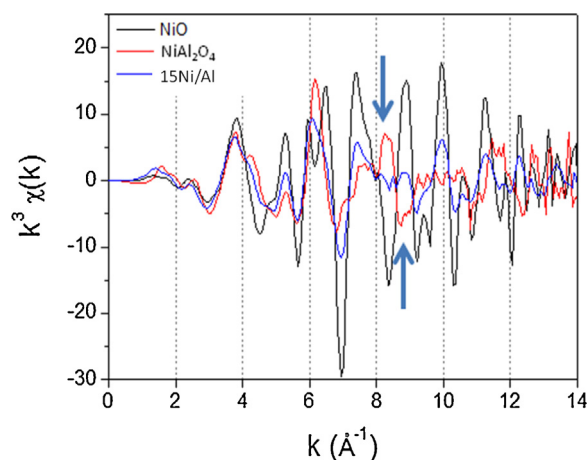


**Fig. 4.**  $k^3$  weighted EXAFS spectra in  $k$  space of NiO, NiAl<sub>2</sub>O<sub>4</sub> and 15Ni/Al.



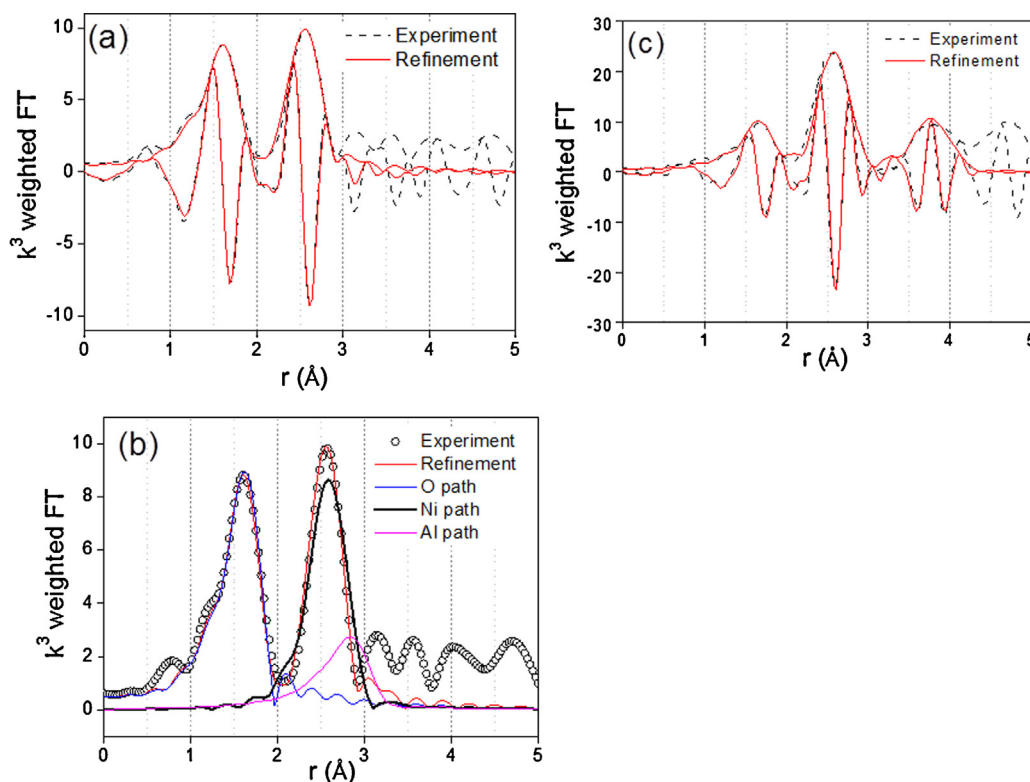


**Fig. 5.**  $k^3$  weighted FT EXAFS, (a) experimental and refined module and imaginary part of the FT of 15Ni/Al; (b) module of the FT of 15Ni/Al and respective backscattering paths used in the refinement; (c) experimental and refined module and imaginary part of the FT of NiO.

(ii) Ni in a local order similar to  $\text{NiAl}_2\text{O}_4$ , in this case the Ni atoms are distributed in tetrahedral and octahedral sites, since  $\text{NiAl}_2\text{O}_4$  is a spinel  $\text{AB}_2\text{O}_4$  [49].

The refinements for 15Ni/Al have uncovered that the first coordination shell of Ni is composed of 6 oxygen atoms. However, the Ni–O bond distance of this catalyst,  $2.04 \pm 0.01$  Å, is shorter than that refined for NiO and longer than the crystallographic distance found for the octahedral site of  $\text{NiAl}_2\text{O}_4$  (1.97 Å).

The second peak in the Fourier transformed spectrum (FT) (Fig. 5a) could not be fitted considering just one backscattering path by Ni as scatter, like it was done for NiO (Fig. 5c). According to Fig. 5b, the second peak corresponds to both Ni and Al contributions. In fact, the refinements have shown that this second peak may explain considering 6 Ni atoms at  $2.95 \pm 0.01$  Å and 6 Al atoms at  $3.32 \pm 0.06$  Å. These coordination numbers are the same as those found around the octahedral site of the  $\text{NiAl}_2\text{O}_4$  spinel, whereas the Ni bond distance is the same as the one found for NiO.

The refined structural parameters indicate that the local structure of Ni atoms in the catalyst as a hybrid of NiO and  $\text{NiAl}_2\text{O}_4$ . It seems that NiO was converted to a pre-spinel phase, in which just octahedral sites were found. This may indicate that the octahedral coordination is more stable. Indeed, the temperature required to convert the octahedral sites into tetrahedral was probably not reached.

An *in situ* study may be of interest to better understand the conversion of NiO into  $\text{NiAl}_2\text{O}_4$ . Just slight differences on the local order were found among the catalysts, which shows that the addition of Mg does not play any meaningful role in the local chemical environment of Ni (Table 2).

### 3.1.4. TPR analysis

Analyses of temperature programmed reduction (TPR) were performed to obtain information about the active phase formation

in the studied system aiming to evaluate the effect of the nature of the support on the reduction of nickel, as well as the metal-support interaction. The profile of TPR reduction catalysts are presented in Fig. 6.

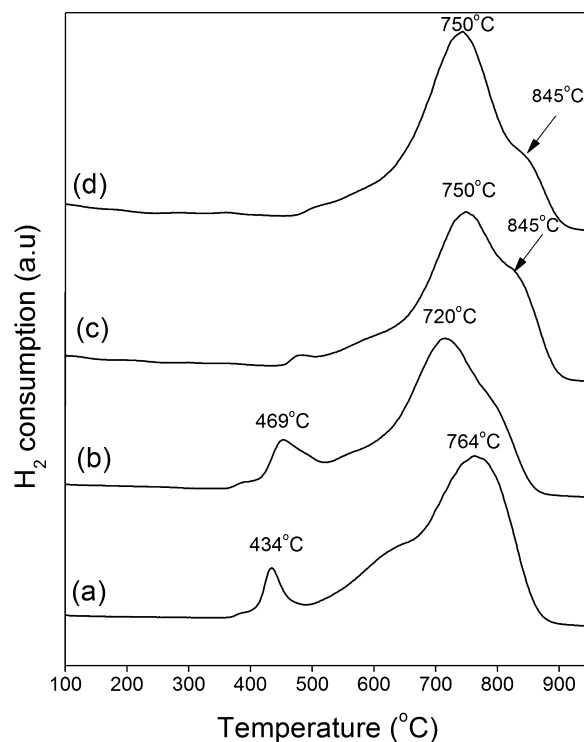


**Fig. 6.**  $\text{H}_2$ -TPR profiles of catalysts (a) 15Ni/Al, (b) 15Ni1Mg/Al, (c) 15Ni5Mg/Al and (d) 15Ni10/Al.

**Table 2**

The refined structural parameters for all catalysts and NiO.

Sample	Atom	N	r (Å)	$\sigma^2 (\times 10^{-3} \text{ Å}^2)$	$\Delta E_0$ (eV)	$\rho$ (%)
15Ni/Al	O	6 <sup>f</sup>	2.04 ± 0.01 <sup>a</sup>	5.7 ± 1.3 <sup>a</sup>	−4.7	1.2
	Ni	6 <sup>f</sup>	2.95 ± 0.01 <sup>a</sup>	7.0 ± 1.0 <sup>a</sup>	± 1.6 <sup>a</sup>	
	Al	6 <sup>f</sup>	3.32 ± 0.06 <sup>a</sup>	12.6 ± 5.5 <sup>a</sup>		
15Ni1Mg/Al	O	6 <sup>f</sup>	2.03 ± 0.01 <sup>a</sup>	5.4 ± 1.1 <sup>a</sup>	−3.8	0.9
	Ni	6 <sup>f</sup>	2.95 ± 0.01 <sup>a</sup>	6.9 ± 1.1 <sup>a</sup>	± 1.6 <sup>a</sup>	
	Al	6 <sup>f</sup>	3.29 ± 0.06 <sup>a</sup>	12.7 ± 5.1 <sup>a</sup>		
15Ni5Mg/Al	O	6 <sup>f</sup>	2.04 ± 0.01 <sup>a</sup>	5.4 ± 1.3 <sup>a</sup>	−4.0	1.2
	Ni	6 <sup>f</sup>	2.95 ± 0.01 <sup>a</sup>	7.5 ± 1.2 <sup>a</sup>	± 1.5 <sup>a</sup>	
	Al	6 <sup>f</sup>	3.32 ± 0.5 <sup>a</sup>	11.7 ± 4.7 <sup>a</sup>		
15Ni10Mg/Al	O	6 <sup>f</sup>	2.03 ± 0.01 <sup>a</sup>	5.8 ± 0.6 <sup>a</sup>	−4.7	1.3
	Ni	6 <sup>f</sup>	2.94 ± 0.01 <sup>a</sup>	7.0 ± 1.0 <sup>a</sup>	± 1.7 <sup>a</sup>	
	Al	6 <sup>f</sup>	3.32 ± 0.06 <sup>a</sup>	12.6 ± 5.6 <sup>a</sup>		
NiO	O	6 <sup>f</sup>	2.08 ± 0.01 <sup>a</sup>	4.2 ± 1.9 <sup>a</sup>	−2.81	0.16
	Ni	12 <sup>f</sup>	2.95 ± 0.01 <sup>a</sup>	6.5 <sup>a†</sup>	± 1.2 <sup>a</sup>	
	O	8 <sup>f</sup>	3.49 ± 0.06 <sup>a</sup>	10.4 ± 5.2 <sup>a</sup>		
	Ni	6 <sup>f</sup>	4.26 ± 0.03 <sup>a</sup>	6.7 ± 3.80 <sup>a</sup>		

Amplitude reduction factor: 0.829, f: fixed parameter, a: refined parameter.

\*Associated uncertainty lower than 10%.

The species of NiO reducible are generally divided into three types:  $\alpha$ ,  $\beta$  and  $\gamma$  [50]. The reduction peak located at low temperature (300–500 °C) can be attributed to the species of the type  $\alpha$ , with little or no interaction with the  $\gamma$ -Al<sub>2</sub>O<sub>3</sub>. These  $\alpha$  species were mainly responsible for Ni sintering and coke formation in the reforming of hydrocarbons [51]. The peak located between the temperatures at 500 °C and 700 °C is assigned the species type  $\beta$ . In addition, the reduction peak located between 700 °C and 900 °C is related to the species of type  $\gamma$ , referring to nickel aluminate (NiAl<sub>2</sub>O<sub>4</sub>) or nickel oxide in strong interaction with the support. Considering these factors, is observed that the catalyst 15Ni/Al and 15Ni1Mg/Al (Fig. 6a and b), has two main reduction peaks. The peaks at 434 °C and 469 °C for 15Ni/Al and 15Ni1Mg/Al catalysts, respectively, can be attributed to the species type  $\alpha$ . In addition, all catalysts that showed the peaks at around 750 °C and 845 °C could be assigned as the reduction of mixed nickel-magnesium or nickel aluminate [52–54]. It is interesting to notice that for the 15Ni5Mg/Al and 15Ni10Mg/Al catalysts, no reduction peaks in the lower temperature (~434 and 460 °C) region were observed (Fig. 6c and d), suggesting that there is no “free” nickel oxide. These results suggest that there is electron transfer from NiO to MgO involving strong interactions between NiO and MgO and decreasing the reducibility of NiO [55,56].

In addition, the TPR results corroborate the EXAFS data, which showed the formation of a pre-spinel phase. This phase required high temperature of reduction, as outlined by TPR data. The incorporation of Ni<sup>2+</sup> ions within the spinel-type structure, during the thermal treatment, may contribute to high dispersion of the active nickel species. Therefore, leading to a good compromise between stability and catalytic activity [57,58]. Spinel materials are known for their high thermal stability; consequently they are widely employed in high-temperature catalytic application such as steam reforming [59], desulfurization [60], among others.

From these results one should highlight that the determination of local, by XAS for example, during the preparation of the catalyst is an important step toward the design of catalysts able to respond to the desirable catalytic properties.

### 3.1.5. Specific surface area (BET)

Specific surface area and pore volume of the supports, as well as the catalysts, are shown in Table 1. As shown in Table 1 the BET surface area and total pore volume of the 15Ni/Al catalyst resulted in considerable decrease compared to the support ( $\gamma$ -Al<sub>2</sub>O<sub>3</sub>). This can be explained due to Ni species that might be mainly located on

the inner surface of the pores of the  $\gamma$ -Al<sub>2</sub>O<sub>3</sub> supports. In addition, BET surface area and the total pore volume of the catalysts promoted with Mg decrease with the increase of magnesium content (Table 1), probably due to blockage of the support pores.

### 3.1.6. High resolution transmission electron microscopy (HRTEM)

To analyze the effect of adding magnesium on the morphology of the catalysts and evaluate the particle size distribution, TEM analyses were performed on the 15Ni/Al and 15Ni5Mg/Al samples before, after the activation process at 750 °C and after reaction at 600 °C. Fig. 7 shows the images obtained by transmission electron microscopy and the histograms of the particle size distributions obtained from the count of the least 50 units, using the software ImageJ 1.47v. From the statistical analysis it was observed that the catalyst 15Ni/Al has an average particle size of 15.16 ± 5.01 nm. However, the 15Ni5Mg/Al catalyst showed an average particle size of 9.27 ± 3.27 nm. Considering the variation involved, determined by the standard deviation, it is observed that the values determined by HRTEM and XRD for crystallite size are equivalent (Table 1).

These results, associated with XRD data, show that the addition of Mg prevents sintering of Ni particles on the catalysts surface, besides preventing agglomeration thereof. According to Barsoun 1997 [61], the reduction of excess energy on the material surface is the factor responsible for the sintering process. This reduction in energy can occur by reducing the surface area, through increased average particle size or by creating an area of grain boundaries in which the grains grow (leading to densification), since these two mechanisms can compete between themselves. The sintering geometry proposed by German 1996 [62] shows that bonds created with the sintering become evident as the contact area between the particles increases. This phenomenon can be observed through the micrograph obtained by high resolution transmission electron microscopy of the 15Ni/Al catalyst, in which the process of Ni particle sintering is observed, as can be seen highlighted in Fig. 8.

## 3.2. Catalytic tests

### 3.2.1. Acetic acid steam reforming

Detailed acetic acid conversion and carbon formed over all catalysts in the steam reforming of acetic acid at 500 °C and 600 °C after 6 h of reaction are summarized in Table 3. According to Table 3 all catalysts showed conversion above 90% for acetic acid at 500 °C and 600 °C. It is noteworthy that the addition of magnesium as promoter did not affect the conversion of acetic acid. According

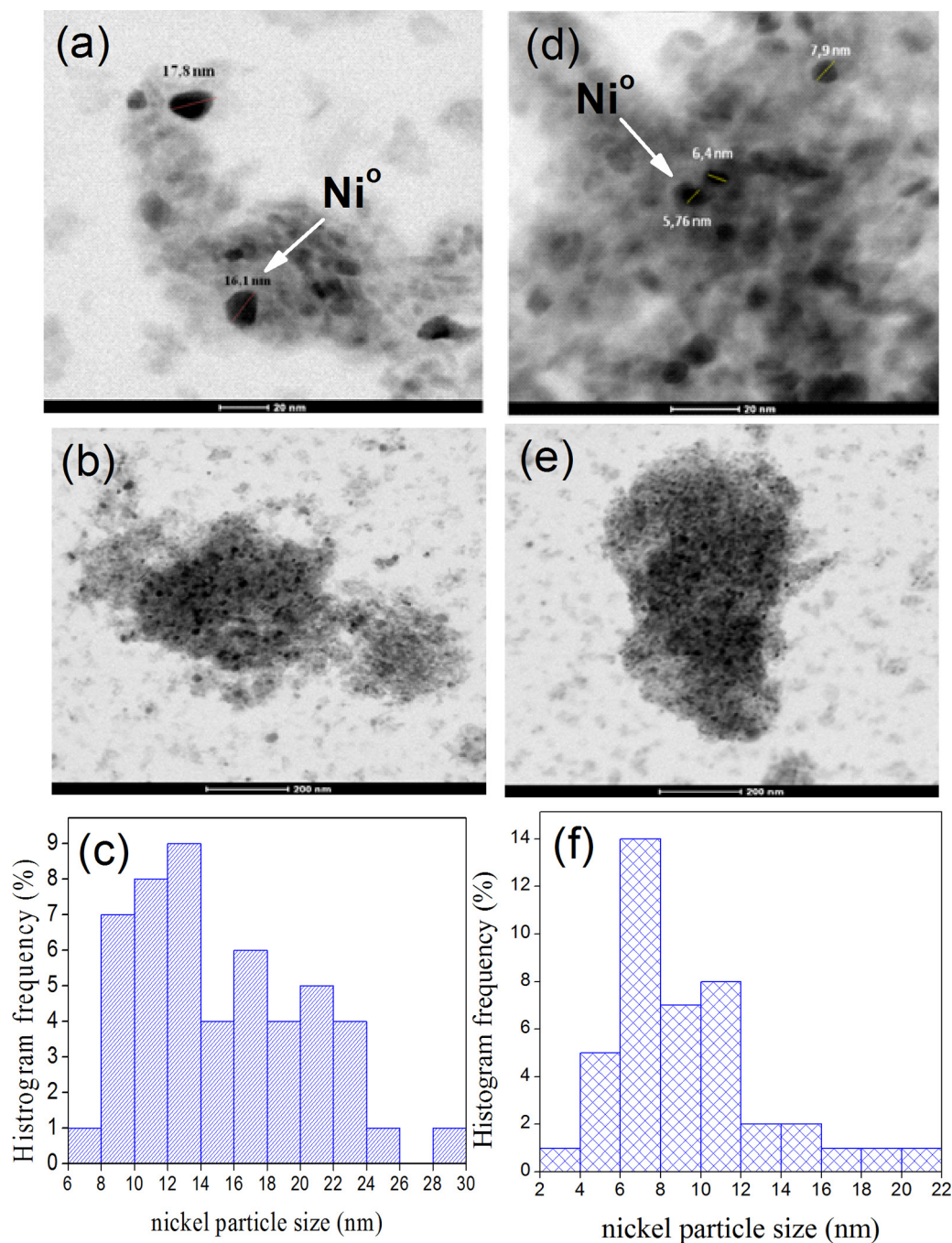


**Fig. 7.** HRTEM images of catalysts after reduction process at 750 °C, (a) 15Ni/Al (20 nm), (b) 15Ni/Al (200 nm), (c) histogram frequency for 15Ni/Al, (d) 15Ni5Mg/Al (20 nm), (e) 15Ni5Mg/Al (200 nm) and histogram frequency for 15Ni5Mg/Al.

to Davidian et al. [63] acetic acid is fully converted at temperatures above 300 °C. The authors also concluded that at temperatures less than 500 °C the carbon deposition reaction is predominant and the formation of gaseous products such as H<sub>2</sub>, CO and CO<sub>2</sub> becomes

**Table 3**  
Conversion of acetic acid at (a) 500 °C and (b) 600 °C after 6 h of reaction and carbon deposition rate (mmol h<sup>-1</sup>).

Catalysts	Conversion (%)		Coke	
	500 °C	600 °C	500 °C mmol C/h	600 °C mmol C/h <sup>-1</sup>
15Ni/Al	98	93	0.103	0.079
15Ni1Mg/Al	94	97	0.125	0.088
15Ni5Mg/Al	96	96	0.114	0.057
15Ni10Mg/Al	92	93	0.112	0.050

relevant from 600 °C. The steam reforming of acetic acid reaction occurs according to Eq. (1). In the conversion of acetic acid, side reactions may also occur, for example, the water-gas shift (Eq. (3)), thermal decomposition (Eqs. (4A)–(4C)) and ketonization reactions (Eq. (5)).

- water-gas shift reaction



- thermal decomposition





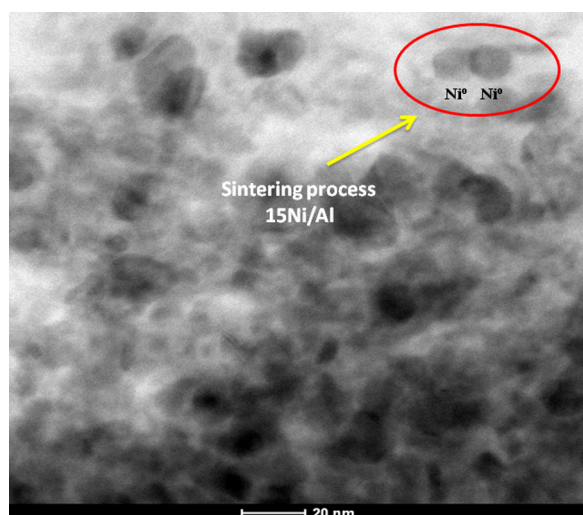
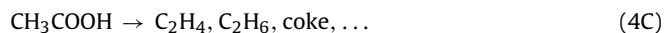


Fig. 8. HRTEM images of 15Ni/Al catalyst (sintering process).



- ketonization

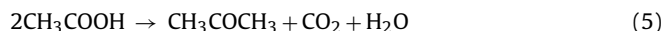


Fig. 9 shows the selectivity for  $\text{H}_2$  and  $\text{CO}_2$  for 15Ni/Al, 15Ni1Mg/Al, 15Ni5Mg/Al and 15Ni10Mg/Al catalysts during 6 h of reaction. As can be seen from Fig. 9a, the presence of the MgO did not enhance the reforming reaction at  $500^\circ\text{C}$ , showing a similar selectivity for  $\text{H}_2$  (~50%) in time-on-stream for 15Ni/Al and

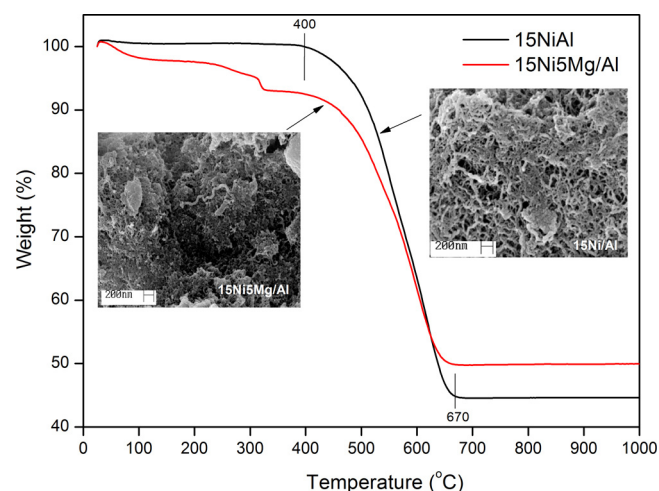


Fig. 10. Selectivity for  $\text{CO}$  and  $\text{CH}_4$  at  $500^\circ\text{C}$  and  $600^\circ\text{C}$  for all catalysts.

15Ni5Mg/Al catalysts. The 15Ni1Mg/Al and 15Ni10Mg/Al catalysts showed selectivity of 40% and 27% for hydrogen, respectively. As shown in Fig. 9a and b the 15Ni1Mg/Al catalyst was less selective for  $\text{H}_2$ , when compared to the catalysts 15Ni/Al and 15Ni5Mg/Al.

The different performance between catalysts can be assigned to the low Mg content in the 15Ni1Mg/Al catalyst, which is not able to suppress carbon deposition over its surface (see Table 3). Moreover, the addition of Mg decreases the ability of Ni catalyst for  $\text{CH}_4$  decomposition [64]. Fig. 10a shows that the addition of 1 and 5% of Mg increases  $\text{CH}_4$  selectivity at  $500^\circ\text{C}$ . The presence of methane is undesirable, in which each mole of  $\text{CH}_4$  formed, 4 moles of  $\text{H}_2$  can

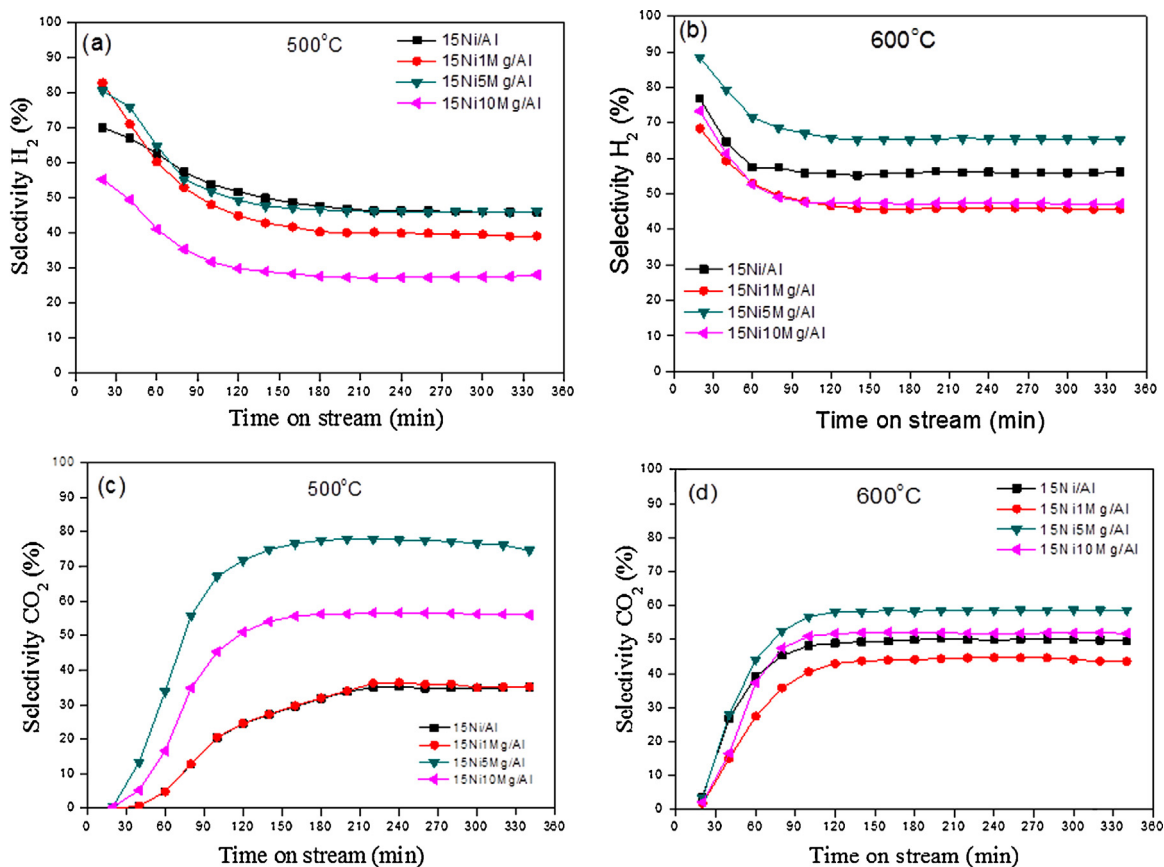


Fig. 9. Selectivity for  $\text{H}_2$  and  $\text{CO}_2$  at  $500^\circ\text{C}$  and  $600^\circ\text{C}$  for all catalysts.



be consumed. Although the 15Ni5Mg/Al catalyst has shown high CH<sub>4</sub> selectivity, during the reforming reaction, carbon deposition was highly suppressed by addition of 5% of Mg, this behavior is more evident at 600 °C. This suggests that in the presence of the promoters the formed coke did not block the nickel surface for the reaction, avoiding the deactivation. The main causes of deactivation ascribed to nickel catalysts used in reforming processes are the loss of active surface by metal sintering and coke deposition [65]. Carvalho and co-workers [46] studied the preparation of catalysts with aluminum and magnesium oxides-supported ruthenium for steam reforming methane. The authors conclude that the addition of small amounts of magnesium to alumina-supported ruthenium in the range of Mg/Al (molar) = 0.2–0.5 did not change the gamma-alumina structure. Nevertheless, the addition of low amounts of magnesium (Mg/Al = 0.2–0.5) showed the highest dispersions, but led to low methane conversions. Moreover, the hydrogen to carbon monoxide molar ratios were quite different for the catalysts, wherein the sample with the molar ratio Mg/Al = 0.2 showed the lowest ratio compared to the catalyst without magnesium and catalyst with molar ratio Mg/Al = 5. It can be assigned to the presence of electron deficient ruthenium species observed in the catalyst with low magnesium content (Mg/Al = 0.2), which are less active for the water gas shift reaction. According to Miguel et al. [66] the physical properties of  $\gamma$ -Al<sub>2</sub>O<sub>3</sub> are slightly changed by the addition of low alkali metal concentrations. Alkali metals are adsorbed selectively on tetrahedral Lewis Al<sup>3+</sup> sites of the alumina surface. These effects on the tetrahedral cations are more marked with increasing molar concentration and ionic radius of the alkali metal added to Al<sub>2</sub>O<sub>3</sub>. The authors conclude that the influence of alkali metals is not only due to steric factors, but also due to possible electronic modifications, improving the stability of Al<sub>2</sub>O<sub>3</sub> and avoiding nickel sintering. This means that the support and load of Mg is playing a role in determining the catalytic activity, in accordance with other works [67].

Methane present in the gaseous effluent may originate from thermal decomposition of acetic acid according to Eq. (4B). Another possible route for the production of methane from acetic acid is the presence of a secondary reaction, such as methanation reactions (Eqs. (6) and (7)) [68]. The methanation reactions are highly favorable for steam reforming processes, since gaseous effluents are rich in hydrogen, carbon monoxide and carbon dioxide [69,70].



Is important to note that the low selectivity for H<sub>2</sub> to the 15Ni10Mg/Al catalyst, was probably due to the coating of the pores of alumina by the addition of magnesium, thereby reducing the access of reactants to the active sites [71]. This result corroborates with the data of surface area (BET), where the addition of 10% magnesium, reduce the surface area of the 15Ni10Mg/Al catalyst by 25% compared to the 15Ni/Al catalyst. In agreement with these results, there is the work of Dieuzeid et al. [72], in which the authors observed similar behavior for catalysts containing nickel supported on alumina and promoted with Mg for steam reforming of glycerol. The authors found that the addition of the higher Mg load (~15) significantly reduced the catalytic activity, thus decreasing the selectivity for H<sub>2</sub>. Furthermore, there was a decrease in the selectivity for hydrogen in the first minutes of reaction, whereas the equilibrium was reached only after 90 min of reaction, keeping the selectivity for hydrogen at approximately 50% for both catalysts. The deactivation in the first minutes of reaction for all catalysts can be explained by coke formation on the catalysts surface [73]. Coke

formation on the catalyst can occur through the Boudouard reaction (Eq. (8))



This phenomenon is evident when the increase of the selectivity for CO<sub>2</sub> is observed during the first 90 min of reaction (Fig. 9c), this increase is also from the Boudouard reaction.

At 600 °C an increase was observed in selectivity for H<sub>2</sub> for all catalysts (Fig. 9b). This behavior is expected, since the reforming reactions in general, are endothermic processes. In addition, the CH<sub>4</sub> formed during steam reforming of acetic can be converted into H<sub>2</sub>, since the methane is the favored product at lower temperatures, with hydrogen being preferred at high temperatures [74,75]. Among the tested materials, the 15Ni5Mg/Al catalyst showed better activity for H<sub>2</sub> compared to the others. In the first minutes of reaction the 15Ni5Mg/Al catalyst showed 87% selectivity for H<sub>2</sub>. However, after 120 min of reaction the 15Ni5Mg/Al catalyst showed a gradual deactivation, reaching around 65% selectivity for H<sub>2</sub>, remaining constantly the same until the end of reaction. Similar behavior was observed for the non-promoted catalyst (15Ni/Al), but with less selectivity for H<sub>2</sub>. The best catalytic activity for the 15Ni5Mg/Al catalyst can be attributed to the smaller particle size and the dispersion metallic of nickel. Furthermore, the 15Ni5Mg/Al catalyst showed a lower amount of coke when compared with the 15Ni/Al catalyst. It is also important to note that large Ni particles can accelerate the rate of carbon deposition on the catalysts [76]. On the other hand, the carbon adsorbed on the small Ni particles diffuses with more difficulty than on the large Ni particles, decreasing the rate of deposited carbon [77].

According Garcia-Vargas et al. [78] the particle size of Ni and metallic dispersion are the key factors for the formation of carbon deposition, in which larger particles of nickel accelerate the rate of coke deposition on the materials surface. On the other hand, the coke adsorbed on small nickel particles diffuses with greater difficulty than that on larger particles, thereby decreasing the coke deposition rate. It is important to note that at 600 °C, the coke amount reduced significantly (Table 3). This behavior can be understood by analyzing the thermograms (TG) for the 15Ni/Al and 15Ni5Mg/Al catalysts (Fig. 11). The carbon oxidation begins at between 400 °C and ends at 670 °C for the 15Ni/Al catalyst. For the 15Ni5Mg/Al catalyst the carbon oxidation begins at between 100 °C and ends at 670 °C. Thus, at 500 °C the majority of the carbon formed remains on the catalyst surface. However, at 600 °C the carbon formed is oxidized, reducing the amount of coke. In addition, the TG analysis of 15Ni/Al and 15Ni5Mg/Al catalysts showed some difference concerning the gasification temperature of coke formed during acetic acid steam reforming. TG analyses can be employed as a complementary technique for evaluation of the structural order of carbon deposits, since the more ordered the carbon structure, the higher will be the temperature for gasification [79,80]. Fig. 11b displays the derivative thermogram, where it can be observed that oxidation of carbon deposits for 15Ni5Mg/Al started at low temperature. The peak appearing up to about 350 °C is assigned to the thermal desorption of H<sub>2</sub>O and CO<sub>2</sub> and removal of easily oxidizable carbonaceous species like an amorphous type. Above 500 °C, the high weight loss can be assigned to the graphitic or filamentous carbon oxidation [81,82].

This fact may suggest a role of MgO in catalyzing the combustion of the deposited carbon, where the addition of magnesium favors coke removal by gasification [83]. It has been proposed that the MgO enhances the rate of H<sub>2</sub>O dissociation, which results in higher amounts of OH<sub>y</sub> species (spill-over effect) on the surface of nickel, besides improving the interaction of surface-adsorbed carbon with gas phase oxygen, leading to the formation of a CO precursor species. The CO formation on these catalysts could be related to a contribution of carbon removal reactions such as the reverse of

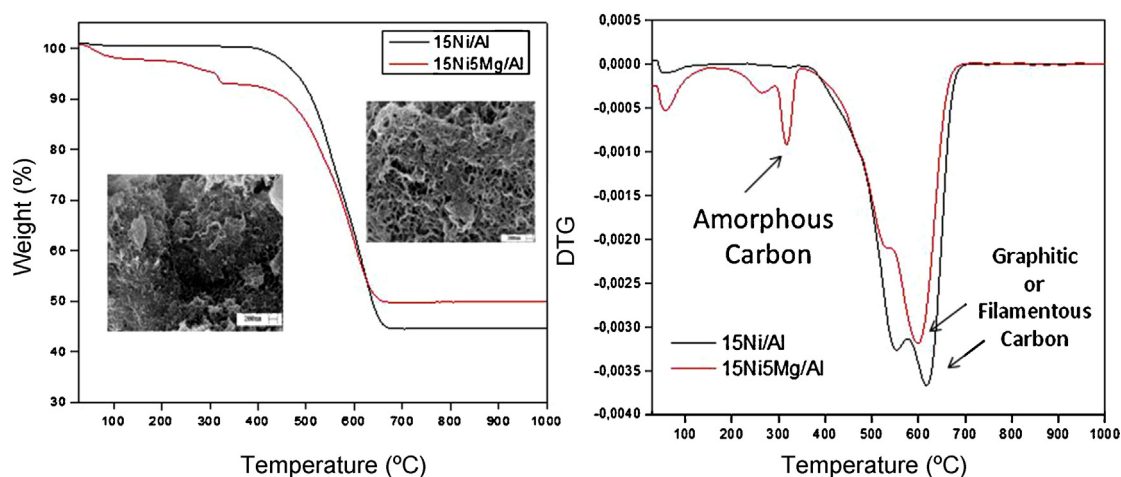


**Fig. 11.** (a) TGA of used 15Ni/Al (inset, SEM micrographs of 15Ni/Al catalyst after reaction) and 15Ni5Mg/Al (inset, SEM micrographs of 15Ni5Mg/Al catalyst after reaction) catalysts performed under airflow and (b) derivative thermograms for used 15Ni/Al and 15Ni5Mg/Al catalysts.

the Boudouard reaction (Eq. (9)), the  $C_{(A)}$  being amorphous carbon ( $\Delta G^{\circ}_{600^{\circ}\text{C}} = -4.4 \text{ kJ mol}^{-1}$ ) [84].



According to Galletti et al. [85] at high-temperatures the reverse of the Boudouard reaction is favored, thereby contributing to the reduction of coke on the catalysts. These results are in line with

the catalytic data shown in Fig. 10d, in which there is an increase in selectivity for CO for all catalysts at 600 °C. Other authors have indicated that the addition of magnesium caused the formation of more easily oxidized coke [86].

So, in an attempt to clarify the interaction between Ni particles and carbon deposits in the 15Ni/Al and 15Ni5Mg/Al catalysts, TEM images of the use catalysts were taken and shown in Fig. 12. The

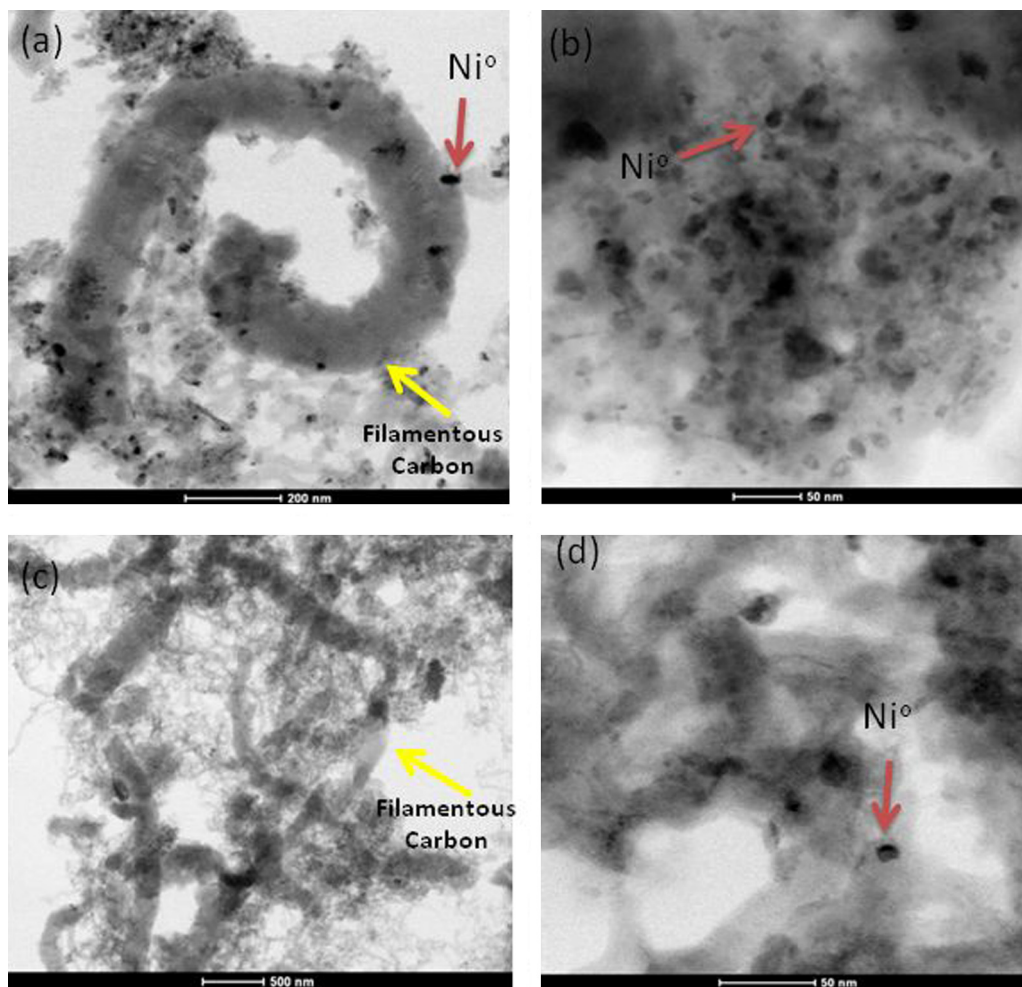


**Fig. 12.** HRTEM images of catalysts after reaction at 600 °C: 15NiAl (Figs. a and b) 15Ni5Mg/Al (Figs. c and d).

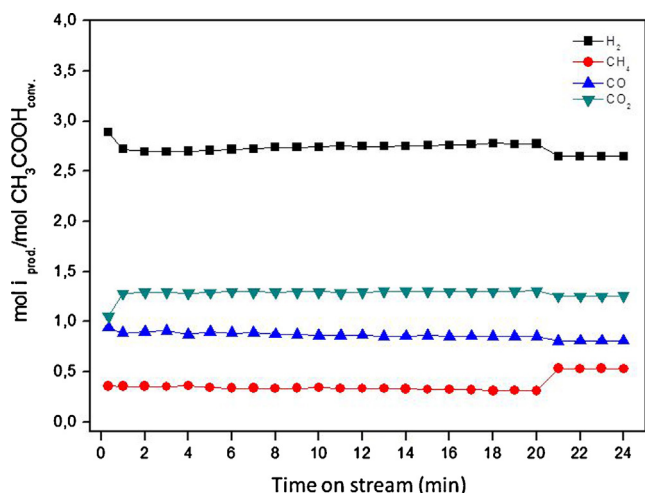


Fig. 13. Stability test for 15Ni5Mg/Al catalyst at 600 °C for a period of 24 h.

catalysts showed different types of carbonaceous species formed on the catalyst. The encapsulated carbon and filamentous carbon were observed for both catalysts. Regarding the Ni particle size following the same trend observed for the reduced catalysts at 750 °C, they were larger on the 15Ni/Al catalyst (Fig. 12), with diameter between 14 and 30 nm and smaller for the 15Ni5Mg/Al catalyst 9 and 15 nm. The mean nickel particles diameter directly measured in the HRTEM showed that the mean particle size for 15Ni5Mg/Al catalyst was 11 nm and the 15Ni/Al catalysts was 21 nm, thus confirming slight metal sintering during acetic acid steam reforming.

### 3.2.2. Stability test

In order to investigate the stability of the catalyst during the steam reforming of acetic acid, time-on-stream experiments were performed at 600 °C for the 15Ni5Mg/Al catalyst for a period of 24 h and the results are displayed in Fig. 13. Fig. 13 shows the selectivity for H<sub>2</sub>, CO<sub>2</sub>, CO and CH<sub>4</sub> over the 15Ni5Mg/Al catalyst for 24 h. The conversion of acetic acid was 91% during 24 h on stream at 600 °C. The amount of coke deposited on 15Ni5Mg/Al catalyst was 0.060 mmolC/h. Similar to the amount of coke present during 6 h on stream. In addition, it can be seen that the selectivity of the products over the 15Ni5Mg/Al catalyst at 600 °C were relatively stable during the 24 h on stream. It is interesting to note that the selectivity of CO remains almost unaffected during the 24 h on stream operation.

## 4. Conclusion

Through analysis of X-ray diffractometry it was observed that with increased Mg load in the catalysts, the main diffraction peaks of  $\gamma$ -Al<sub>2</sub>O<sub>3</sub> shift to a small angle, due to the formation of the MgAl<sub>2</sub>O<sub>4</sub> phase. This effect is more evident in the 15Ni5Mg/Al and 15Ni10Mg/Al catalysts. The EXAFS analyses corroborate the XRD findings. The local chemical environment of Ni after calcination may be described as Ni aluminate phase. It was observed that the addition of Mg in the calcined catalysts does not play any meaningful role on the local chemical environment of Ni. Moreover, the histograms obtained from the analysis of high resolution transmission electron microscopy showed that 15Ni/Al catalyst has non-homogeneous distribution with an average particle size of 15 nm and that with the addition of 5 wt.% Mg, the average particle size decreases to 9.5 nm. This shows that addition of Mg prevents the nickel particle sintering process on the catalyst surface. In addition, the presence of MgO did not enhance the reforming reaction at 500 °C showing a similar selectivity for H<sub>2</sub> in

time-on-stream for 15Ni/Al and 15Ni5Mg/Al catalysts. However, at 600 °C the 15Ni5Mg/Al catalyst was more selective for production of hydrogen and in addition showed high stability for reforming of acetic acid during 24 h on stream. The promotional effect of MgO may be attributed to sintering resistance ability and low acidity of MgAl<sub>2</sub>O<sub>4</sub> compared to  $\gamma$ -Al<sub>2</sub>O<sub>3</sub> and the interactions between Ni and MgAl<sub>2</sub>O<sub>4</sub> were assumed to be responsible for its high activity and resistant to coking.

## Acknowledgements

The authors thank the Brazilian National Council for Scientific Development (CNPq) and the Brazilian Synchrotron Light Laboratory (LNLS) in Campinas, Brazil, for the XAS analysis.

## References

- [1] M.A. Mujeebua, M.Z. Abdulla, M.Z. Abu Bakar, A.A. Mohamad, R.M.N. Muhad, M.K. Abdullah, *J. Environ. Manage.* 90 (2009) 2287.
- [2] Y.H.P. Zhang, *Int. J. Hydrogen Energy* 35 (2010) 10334.
- [3] J.-J. Zoua, Y.-P. Zhang, C.-J. Liu, *Int. J. Hydrogen Energy* 32 (2007) 958.
- [4] J. Brouwer, *Curr. Appl. Phys.* 10 (2010) S9.
- [5] B. McLellan, E. Shoko, A.L. Dicks, J.C.D. Costa, *Int. J. Hydrogen Energy* 30 (2005) 669.
- [6] R.J. Farrauto, *Appl. Catal. B* 56 (2005) 3.
- [7] Z. Wang, Y. Pana, T. Donga, X. Zhua, T. Kana, L. Yuana, Y. Torimoto, M. Sadakata, Q. Li, *Appl. Catal. A* 320 (2007) 24.
- [8] R. Shinnar, *Technol. Soc.* 25 (2003) 455.
- [9] C.C.R.S. Rossia, C.G. Alonso, O.A.C. Antunes, R. Guirardello, L. Cardozo-Filho, *Int. J. Hydrogen Energy* 34 (2009) 323.
- [10] R. Chandra, H. Takeuchi, T. Hasegawa, *Renew. Sust. Energy Rev.* 16 (2012) 1462.
- [11] A.V. Bridgwater, *Biomass Bioenerg.* 38 (2012) 68.
- [12] L. García, R. French, S. Czernik, E. Chornet, *Appl. Catal. A* 201 (2000) 225.
- [13] T. Chen, C. Wu, R. Liu, *Bioresour. Technol.* 102 (2011) 9236.
- [14] J.A. Medrano, M. Oliva, J. Ruiz, L. García, J. Arauzo, *Energy* 36 (2011) 2215.
- [15] S. Czernik, R. Evans, R. French, *Catal. Today* 129 (2007) 265.
- [16] Z. Lia, X. Hua, L. Zhang, G. Lua, J. Mol. Catal. A: Chem. 355 (2012) 123.
- [17] P.G.M. Assaf, F.G.E. Nogueira, E.M. Assaf, *Catal. Today* 213 (2013) 2.
- [18] F. Bimbela, M. Oliva, J. Ruiz, L. García, J. Arauzo, *J. Anal. Appl. Pyrolysis* 79 (2007) 112.
- [19] A.C. Basagiannis, X.E. Verykios, *Appl. Catal. B* 82 (2008) 77.
- [20] J.A.Z. Pieterse, J. Boon, Y.C. van Delft, J.W. Dijkstra, R.W. Van den Brink, *Catal. Today* 156 (2010) 153.
- [21] S.Q. Chen, Y. Liu, *Int. J. Hydrogen Energy* 34 (2009) 4735.
- [22] G. Wu, S. Lia, C. Zhanga, T. Wang, J. Gong, *Appl. Catal. B* 144 (2014) 277.
- [23] M.C. Sánchez-Sánchez, R.M. Navarro, J.L.G. Fierro, *Int. J. Hydrogen Energy* 32 (2007) 1462.
- [24] V.R. Choudhary, B.S. Uphade, A.S. Mamman, *J. Catal.* 172 (1997) 281.
- [25] D.S. Maciver, H.H. Tobim, R.T. Barth, *J. Catal.* 2 (1963) 485.
- [26] A. Boumanza, L. Favaro, J. Lédion, G. Sattouay, J.B. Brubach, P. Berthet, A.M. Huntz, P. Roy, R. Tétot, *Solid State Chem.* 182 (2009) 1171.
- [27] J.M. Bermúdez, B. Fidalgo, A. Arenillas, J.A. Menéndez, *Fuel* 94 (2012) 197.
- [28] D. Chen, R. Lodeng, A. Anundskas, O. Olsvik, A. Holmen, *Chem. Eng. Sci.* 56 (2001) 1371.
- [29] A.J. Vizcaino, M. Lindo, A. Carrero, J.A. Calles, *Int. J. Hydrogen Energy* 37 (2012) 1985.
- [30] H. Klung, L. Alexander, *X-ray Diffraction Procedures*, Wiley, New York, USA, 1962, pp. 491.
- [31] B. Ravel, M. Newville, *J. Synchrotron Radiat.* 12 (2005) 537.
- [32] J. Guo, H. Lou, H. Zhao, D. Chai, X. Zheng, *Appl. Catal. A* 273 (2004) 75.
- [33] S. Calvin, E.E. Carpenter, B. Ravel, V.G. Harris, *Phys. Rev. B* 66 (2002) 224405.
- [34] K.F. Waldner, R.M. Laine, S. Dhumrongvaraporn, S. Tayaniphan, N. Narayanan, *Chem. Mater.* 8 (1996) 2850.
- [35] B. Vos, E. Poels, A. Bliek, *J. Catal.* 198 (2001) 77.
- [36] P. Kim, Y. Kim, H. Kim, I.K. Song, J. Yi, *Appl. Catal. A* 272 (2004) 157.
- [37] E.G. Derouane, V. Jullien-Lardot, R.J. Davis, N. Blom, P.E. Hojlund-Nielsen, *Stud. Surf. Sci. Catal.* 75 (1993) 1031.
- [38] L.K. Kurihara, S.L. Suib, *Chem. Mater.* 5 (1993) 609.
- [39] L. Zhang, W. Li, J. Liu, C. Guo, Y. Wang, J. Zhang, *Fuel* 88 (2009) 511.
- [40] R.A. Couttenye, M.H. Vila, S.L. Suiba, *J. Catal.* 233 (2005) 317.
- [41] L. García, A. Benedicto, E. Romeo, M.L. Salvador, J. Arauzo, R. Bilbao, *Energy Fuels* 16 (2002) 1222.
- [42] A.L. Bonivardi, M.A. Baltanás, *J. Catal.* 138 (1992) 500.
- [43] G. Fagherazzi, A. Benedetti, S. Polizzi, A.D. Mario, F. Pinna, M. Signoretto, N. Pernicone, *Catal. Lett.* 32 (1995) 293.
- [44] D. Xu, W. Li, H. Duan, H. Ge, H. Xu, *Catal. Lett.* 102 (2005) 229–235.
- [45] Y.J.O. Asencios, C.R. Rodella, E.M. Assaf, *Appl. Catal. B* 132 (2013) 1.
- [46] L.S. Carvalho, A.R. Martin, P. Reyes, M. Oportus, A. Albonoz, V. Vicentini, M.C. Range, *Catal. Today* 142 (2009) 52.
- [47] Y. Zhang, Y. Zhou, L. Wan, M. Xue, Y. Duan, X. Liu, *Fuel Process. Technol.* 92 (2011) 1632.

- [48] R.W. Cairns, E. Ott, *J. Am. Chem. Soc.* 55 (1933) 527.
- [49] J.N. Roelofs, R.C. Peterson, M. Raudsepp, *Am. Miner.* 77 (1992) 522.
- [50] K.Y. Koo, H.-S. Roh, Y.T. Seo, D.J. Seo, *Int. J. Hydrogen Energy* 33 (2008) 2036.
- [51] C.H. Bartholomew, *Appl. Catal. A* 212 (2011) 17.
- [52] T. Shishido, M. Sukenobu, H. Morioka, M. Kondo, Y. Wang, K. Takaki, K. Takehira, *Appl. Catal. A* 223 (2002) 35.
- [53] J.T. Richardson, B. Turk, M.V. Twigg, *Appl. Catal. A* 148 (1996) 97.
- [54] W. Chu, W. Yang, L. Lin, *Appl. Catal. A Gen.* 235 (2002) 39.
- [55] F. Basile, L. Basini, M.D. Amore, G. Fornasari, A. Guarinoni, D. Matteuzzi, G. Del Piero, F. Trifiro, A. Vaccari, *J. Catal.* 173 (1998) 247.
- [56] M. Serra, P. Salagre, Y. Cesteros, F. Medina, J.E. Sueiras, *Solid State Ionics* 134 (2000) 229.
- [57] D.G. Rethwisch, J.A. Dumesic, *Appl. Catal. A* 21 (1986) 97.
- [58] S.M. Lima, J.M. Assaf, M.A. Penã, J.L.G. Fierro, *Appl. Catal. A* 311 (2006) 94.
- [59] J.R. Rostrup-Nielsen, *Catal. Today* 71 (2002) 243.
- [60] D.L. Stern, K.E. Nariman, J.S. Buchanan, N.A. Bhole, D.L. Johnson, R.K. Grasselli, *Catal. Today* 5 (2000) 311.
- [61] M.W. Barsoum, *Fundamentals of Ceramics*. McGraw Series in Materials Science and Engineering, Drexel University, 1997.
- [62] R.M. German, *Sintering Theory and Practice*, The Pennsylvania State University, John Wiley & Sons, Inc., 1996, pp. 568.
- [63] T. Davidian, N. Guilhaume, C. Daniel, C. Mirodatos, *Appl. Catal. A* 335 (2008) 64.
- [64] T. Horiuchi, K. Sakuma, T. Fukui, Y. Kubo, T. Osaki, T. Mori, *Appl. Catal. A* 144 (1996) 111.
- [65] R. Trane, S. Dahl, M.S. Skjøth-Rasmussen, A.D. Jensen, *Int. J. Hydrogen Energy* 37 (2012) 6447.
- [66] S.R. Miguel, O.A. Scelza, A.A. Castro, *Top. Catal.* 1 (1994) 87.
- [67] J.T. Richardson, B. Turk, M.V. Twigg, *Appl. Catal. A: Gen.* 148 (1996) 97.
- [68] A.N. Fatsikostas, D.I. Kondarides, X.E. Verykios, *Catal. Today* 75 (2002) 145.
- [69] C.-W. Hu, J. Yao, H.-Q. Yang, Y. Chen, A.-M. Tian, *J. Catal.* 166 (1997) 1.
- [70] I. Czekaj, F. Loviat, F. Raimondi, J. Wambach, S. Biollaz, *Appl. Catal. A* 329 (2007) 68.
- [71] A. Penkova, L. Bobadilla, S. Ivanova, M.I. Domínguez, F. Romero-Sarria, A.C. Roger, M.A. Centeno, J.A. Odriozola, *Appl. Catal. A* 392 (2011) 184.
- [72] M.L. Dieuzeide, M. Jobbagy, N. Amadeo, N. Catal. Today 213 (2013) 50.
- [73] E.Ch. Vagia, A. Lemonidou, *Appl. Catal. A* 351 (2008) 111.
- [74] J.R. Rostrup-Nielsen, *Steam Reforming Catalysts*, Teknisk Forlag, Denmark, 1975.
- [75] M.V. Twigg, *Catalyst Handbook*, 2nd ed., Manson, London, 1994.
- [76] H.T. Jiang, H.Q. Li, H.B. Xu, Y. Zhang, *Fuel Process. Technol.* 88 (2007) 988.
- [77] M. Eizenberg, J.M. Blakely, *Surf. Sci.* 82 (1979) 228.
- [78] J.M. García-Vargas, J.L. Valverde, A. Lucas-Consuegra, B. Gómez-Monedero, P. Sánchez, F. Dorado, *Appl. Catal. A* 431 (2012) 49.
- [79] C. Park, M.A. Keane, *J. Catal.* 221 (2004) 386.
- [80] J. Chen, X. Yang, Y. Li, *Fuel* 89 (2010) 943.
- [81] J. Guo, H. Lou, H. Zhao, D. Chai, X. Zheng, *Appl. Catal. A* 273 (2004) 75–82.
- [82] O.W. Perez-Lopez, A. Senger, N.R. Marcilio, M.A. Lansarin, *Appl. Catal. A* 303 (2006) 234–244.
- [83] N. Alarcón, X. García, M.A. Centeno, P. Ruiz, A. Gordon, *Appl. Catal. A* 267 (2004) 251.
- [84] M.N. Barroso, A.E. Galetti, M.C. Abello, *Appl. Catal. A* 394 (2011) 124.
- [85] A.E. Galetti, M.F. Gómez, L.A. Arrúa, M.C. Abello, *Appl. Catal. A* 348 (2008) 75.
- [86] J.S. Lisboa, D.C.R.M. Santos, F.B. Passos, F.B. Noronha, *Catal. Today* 101 (2005) 15.



**Update**

**Applied Catalysis B: Environmental**

Volume 162, Issue , January 2015, Page 611

DOI: <https://doi.org/10.1016/j.apcatb.2014.07.030>



## Corrigendum

# Corrigendum to “Catalytic steam reforming of acetic acid as a model compound of bio-oil” [Appl. Catal. B: Environ. 160–161 (2014) 188–199]

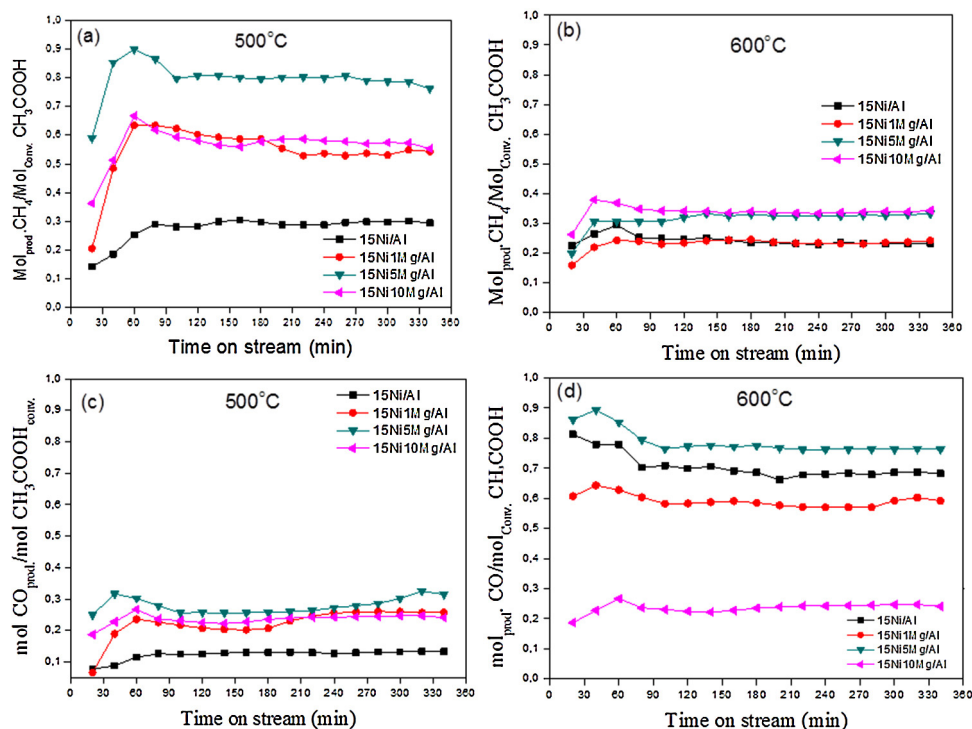
Francisco Guilherme E. Nogueira<sup>a</sup>, Paulo G.M. Assaf<sup>a</sup>,  
Hudson W.P. Carvalho<sup>b</sup>, Elisabete M. Assaf<sup>a,\*</sup>

<sup>a</sup> Instituto de Química de São Carlos, Universidade de São Paulo, Av. Trabalhador São Carlense, 400, 13560-970 São Carlos, SP, Brazil

<sup>b</sup> Institute for Chemical Technology and Polymer Chemistry, KIT, Engesserstrasse 20, 76131 Karlsruhe, Germany



The author regrets that an error appeared in the original paper.  
Artwork of Fig. 10 was incorrect. The corrected version appears below.



DOI of original article: <http://dx.doi.org/10.1016/j.apcatb.2014.05.024>.

\* Corresponding author.

<http://dx.doi.org/10.1016/j.apcatb.2014.07.030>

0926-3373/© 2014 Elsevier B.V. All rights reserved.